Kinetic electron effects in a Hall thruster discharge with a curved magnetic field topology

IEPC-2024-387

Presented at the 38th International Electric Propulsion Conference, Toulouse, France
June 23-28, 2024

Alberto Marín-Cebrián,* Enrique Bello-Benítez †, Eduardo Ahedo ‡
Department of Aerospace Engineering, Universidad Carlos III de Madrid, Leganés, Spain
and
Adrián Domínguez-Vázquez §
Department of Fluid Mechanics, Universidad de Málaga, Málaga, Spain

A two-dimensional particle-in-cell model of the weakly collisional plasma in Hall thruster has been improved to simulate more realistic configurations. The model resolves the axial-radial plane of the discharge, including: (1) a curved magnetic field topology; (2) elastic, excitation and ionization electron-neutral collisions; (3) cylindrical effects; (4) secondary electron emission from the dielectric walls; and (5) a cathode model that ensures continuity of the discharge current at any instant. Since the azimuthal direction is not explicitly simulated, anomalous electron diffusion is included empirically. The use of acceleration techniques, such as a steady-state law for neutrals and an augmented vacuum permittivity, reduced the computational cost. The time evolution of plasma currents to the domain boundaries shows convergence and the steady-state solution is analyzed. The plasma response is strongly affected by the complex magnetic field topology. The curved magnetic field near the anode effectively inhibits the radial plasma motion, reducing particle and energy losses to the walls. The simulation results suggest that the Debye sheaths may collapse for dielectric walls with a grazing magnetic field incidence angle. The comparison with a simulation assuming a purely radial magnetic field completes the discussion. The robustness of the numerical results to variations in different parameters is shown in the appendix.

I. Introduction

Currently, a large part of Hall thruster (HET) research relies on 2D axial-radial (2Dzr) hybrid models,[1,2] treating heavy species (i.e. ions and neutrals) with a particle-in-cell (PIC) formulation and electrons as a drift-diffusive fluid. The standard macroscopic formulation for electrons is based on the assumption that their velocity distribution function (VDF) is (near) Maxwellian.[3] However, the low collisionality in the HET channel prevents the plasma from reaching local thermodynamic equilibrium; and thus, standard fluid models can misrepresent some relevant physics.[4] Alternatively, kinetic models do not make any assumptions on the VDF shape; but the wide range of time and length scales that need to be resolved make multidimensional simulations challenging.[5]

Recently, we have developed a 2Dzr PIC model (PICASO)[6] of the HET discharge to analyze the plasma response. As in many other works in the literature,[7,8] Ref. 6 considered a simplified configuration with a perfectly radial magnetic field. The kinetic solution revealed important differences with respect to standard fluid models: (1) plasma-wall interaction parameters differ largely from classical theory, based on a Maxwellian VDF, (2) the electron heat flux has a complex behavior and cannot be described by a Fourier-type law, and (3) the pressure tensor is composed of a gyrotropic part and small gyroviscous terms. Indeed,

*PhD. candidate, Equipo de Propulsión Espacial y Plasmas (EP2), almarinc@pa.uc3m.es.
†PhD. candidate, Equipo de Propulsión Espacial y Plasmas (EP2), ebello@ing.uc3m.es.
‡Full professor,Equipo de Propulsión Espacial y Plasmas (EP2), eahedo@ing.uc3m.es.
§Associate professor, TEP-997, Equipo de Propulsión Espacial y Plasmas (EP2), adoming@uma.es.

Copyright 2024 by the Electric Rocket Propulsion Society. All rights reserved.

near the anode, gyroviscosity and inertia are relevant in the azimuthal electron momentum equation, where dominant terms are orders of magnitude smaller than in the axial direction. However, the magnetic field topology in real thrusters is curved. Experimental[9,10] and numerical[11,12] works, have shown that oblique magnetic fields can reduce plasma fluxes to the walls and enhance the thruster performances. In other of our previous works,[13] we used a 1D radial (1Dr) PIC model to investigate the effect of a moderately-curved magnetic field in the radial plasma behavior. The kinetic solution showed a significant reduction in electron anisotropy, in agreement with Ref. 14. A magnetic force term, which can be electron confining or expanding, appears in the radial momentum equation and modifies the relative relevance of the radial pressure gradient and electric force density. As a consequence, the plasma density near the wall and the degree of radial ion defocusing were affected. Similar effects were later observed by Reza et al.[15] using a pseudo-2D PIC model.

In this work we extend the model of Ref. 6 to afford the simulation of realistic scenarios including a complex magnetic field topology. The analysis focuses on the steady-state plasma response. The effect of the curved magnetic field on the macroscopic plasma response and plasma-wall interaction magnitudes is discussed. Magnetic field lines are compared against isolines of the thermalized potential, isothermal and isopotential lines. The differences between radial and curved magnetic field cases are addressed as well. Additional simulations are performed to test the robustness of the numerical results.

The article is structured as follows. Section II summarizes the main aspects of the kinetic model. Section III presents and analyzes the simulation results for the reference case. Section IV shows the plasma response in an scenario with a purely radial magnetic field. Finally, conclusions are gathered in Section V.

II. The 2Dzr PIC model

This Section summarizes the the main features of the kinetic code, highlighting the main improvements with respect to Ref. 6. The axisymmetric (i.e. $\partial/\partial\theta = 0$) axial-radial (2Dzr) PIC model (PICASO) aims to solve the plasma response in a Hall thruster discharge taking into account the cylindrical geometry of the

Type	Description and symbol	Value and units
Physical system parameters	Channel inner radius, r_{W1}	54.5 mm
	Channel outer radius, r_{W2}	76.7 mm
	Channel length, L	29 mm
	Anode potential, ϕ_{A}	300 V
	Cathode potential, ϕ_{N}	0
	Mass flow, $\dot{m}$	17.59 mg/s
Surface interaction parameters	Wall cross-over energy, $\mathcal{E}_c$	50 eV
	SEE average emission energy, $\mathcal{E}_{e\mathrm{W}f}$	0.4 eV
	Cathode average emission energy, $\mathcal{E}_{e\mathrm{N}f}$	4.5 eV
Species settings	Initial plasma density, $n_{e0} = n_{i0}$	$4 \cdot 10^{17}$ m^{-3}
	Initial plasma temperature, $T_{e0} = T_{i0}$	1 eV
	Axial neutral velocity, u_{zn}	300 m/s
Numerical parameters	Macroparticle weight, w_p	$6.94 \cdot 10^8$
	Grid spacing, $\Delta z = \Delta r$	200 μm
	Timestep, Δt	15 ps
	Simulated time, t_{sim}	60 μs
	Augmentation factor, f_D	12

Table 1. Reference input parameters for the 2Dzr PIC model.

Copyright 2024 by the Electric Rocket Propulsion Society. All rights reserved.

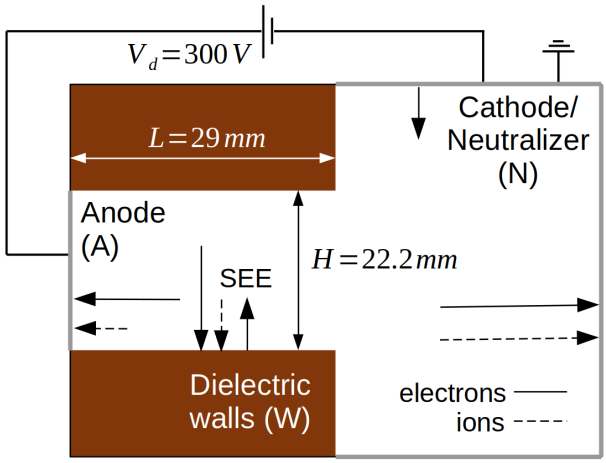

Figure 1. Sketch of the simulation domain. Arrows indicate the the direction of the expected electron (solid lines) and ion (dashed lines) fluxes. The downstream plume boundary also acts as cathode/neutralizer, injecting electrons to satisfy continuity of the discharge current (between anode and cathode) at any instant.

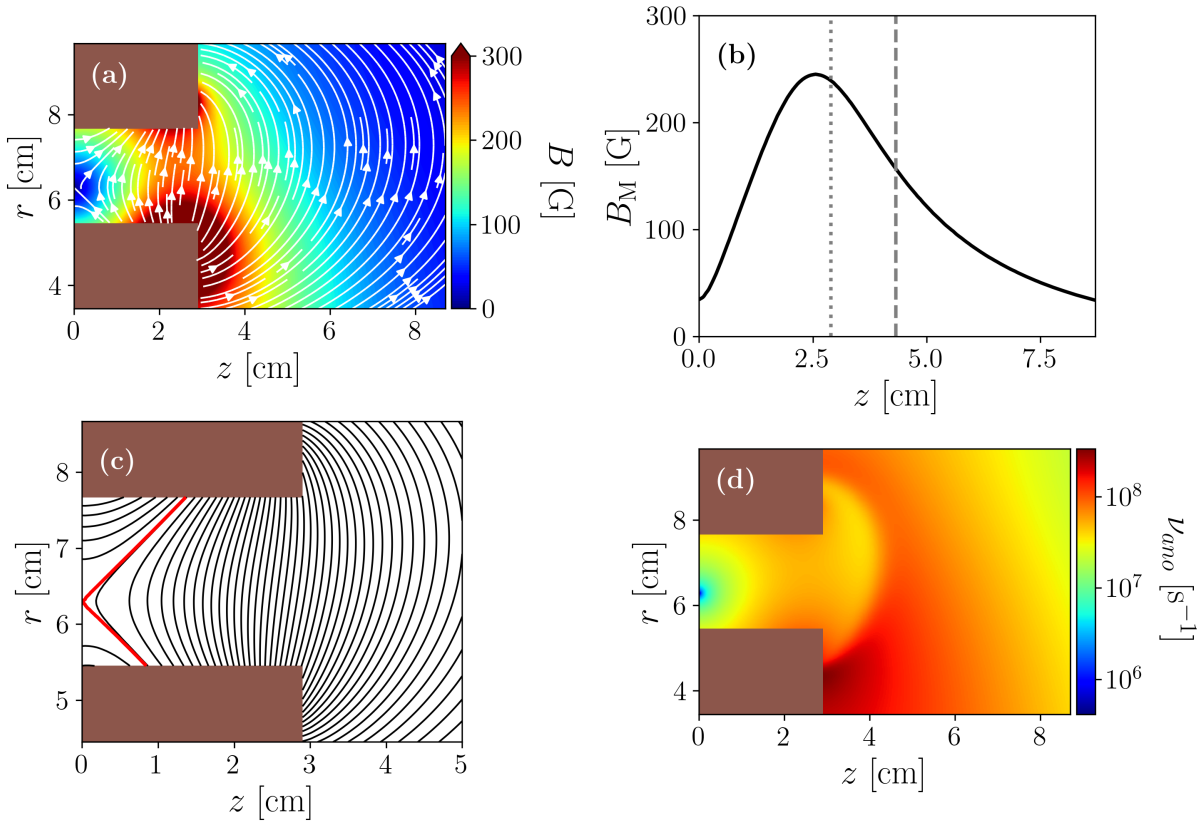

Figure 2. Magnetic field topology for the reference simulation: (a) magnetic field lines, (b) magnetic field magnitude at the mean radius, (c) close up view of the magnetic field lines in the thruster channel. In plot (b) the thruster exit and the anomalous diffusion transition location are marked with dotted and dashed vertical lines respectively. The red line in plot (c) shows the magnetic field line that indicates the approximate transition between magnetic field lines that join the two dielectric walls and those joining one dielectric wall with the anode. The anomalous diffusion map is shown in figure (d).

Copyright 2024 by the Electric Rocket Propulsion Society. All rights reserved.

problem. Figure 1 provides a sketch of the simulation domain, comprising the thruster channel and a small portion of the plume. The domain boundaries are defined by the a metallic anode (A), the dielectric thruster walls (W) and the downstream plume boundary, that acts as the cathode/neutralizer (N). The simulation setup aims to reproduce a virtual 5 kW class HET, similar to Ref. 16. The thruster has dimensions $L = 29$ mm for the channel length and it is bounded by dielectric walls at $r_{\mathrm{W1}} = 54.5$ mm and $r_{\mathrm{W2}} = 76.7$ mm for the inner and outer radii respectively. The simulation domain extends from $z \in [0, 87]$ mm (equivalent to three channel lengths) and $r \in [34.5, 96.7]$ mm (almost three times the channel width). The main input parameters for the kinetic model are summarized in Table 1.

The magnetic field, $\boldsymbol{B}$, is static and externally applied. The magnetic field topology considered is displayed in Fig. 2. Figure 2(a) shows a 2D plot of the magnetic field norm with streamlines and Fig. 2(b) plots the magnetic field magnitude along the channel mean channel radius $B_{\mathrm{M}} = B(z, r_{\mathrm{M}})$, with $r_{\mathrm{M}} = (r_{\mathrm{W1}} + r_{\mathrm{W2}})/2$. The magnetic field is almost radial near the channel exit but it is unconventional in the near anode region, featuring magnetic field lines that are almost parallel to the walls and a singular point. A close up view of the magnetic field lines in the thruster channel is depicted in Fig. 2(c).

The electric field is $\boldsymbol{E} = -\nabla\phi$ and the electric potential, ϕ, is self-consistently obtained from the Poisson equation

$$-\varepsilon\nabla^2\phi = \rho_{el}, \tag{1}$$

where ε is the electric permittivity and ρ_{el} is the electric charge density. Dirichlet boundary conditions are imposed at the anode and cathode surfaces, fixing the discharge potential $V_d = \phi_{\mathrm{A}} - \phi_{\mathrm{N}} = 300$ V, and Neumann conditions are applied at the dielectric walls. The numerical implementation makes use of second order finite differences for the calculation of ϕ and $\boldsymbol{E}$ at the mesh nodes.

Electrons, e, and singly charged xenon ions, i, are simulated as two different populations of macroparticles with constant weight (i.e. number of elementary particles per simulated macroparticle), $w_p \simeq 6.94 \cdot 10^8$ for the simulations shown here. Explicit time integration of particle trajectories is performed using the Boris algorithm.[17] The strict numerical constraints on the cell size and time step imposed by the Debye length and the inverse plasma frequency respectively are relaxed by using an augmented permittivity $\varepsilon = f_D^2\varepsilon_0$, where ε_0 is the vacuum permittivity. For the simulations shown here we apply $f_D = 12$, a common value used in previous works in the literature.[12,18] First-order weighting schemes (Cloud-In-Cell) are used for both, interpolating $\boldsymbol{B}$ and $\boldsymbol{E}$ to the particle position, and calculating integral moments of each species VDF (i.e. the macroscopic magnitudes) at the mesh nodes. The latter are defined as

$$n_s = \iiint f_s \mathrm{d}^3\boldsymbol{v}, \quad n_s\boldsymbol{u}_s = \iiint \boldsymbol{v} f_s \mathrm{d}^3\boldsymbol{v}, \quad \bar{\bar{M}}_s = m_s \iiint \boldsymbol{v}\boldsymbol{v} f_s \mathrm{d}^3\boldsymbol{v}, \quad \boldsymbol{P}_s'' = \frac{m_s}{2}\iiint \boldsymbol{v} v^2 f_s \mathrm{d}^3\boldsymbol{v}, \tag{2}$$

where, f_s is the VDF of species $s = i, e$, n_s is the particle density, $n_s\boldsymbol{u}_s$ is the particle flux vector, $\bar{\bar{M}}_s$ is the momentum flux tensor, and $\boldsymbol{P}_s''$ is the full energy flux vector. Other macroscopic magnitudes are: the current density $\boldsymbol{j}_s = eZ_s n_s \boldsymbol{u}_s$ (with Z_s the charge number), the longitudinal current density $\tilde{\boldsymbol{j}}_s = \boldsymbol{j}_s - j_{\theta s}\boldsymbol{1}_\theta$, the pressure tensor $\bar{\bar{p}}_s = \bar{\bar{M}}_s - m_s n_s \boldsymbol{u}_s\boldsymbol{u}_s$, directional temperatures $T_{xs} = p_{xxs}/n_s$ along $x = z, r, \theta$ and the scalar temperature $T_s = (T_{zs} + T_{rs} + T_{\theta s})/3$. The Extended Weighting Algorithm[19] was used to compute these macroscopic magnitudes at steady-state.

Particles reaching any of the domain boundaries contribute to the electric current to that surface and then removed from the simulation. Additionally, electrons are injected from the neutralizer and secondary electrons are emitted by the dielectric walls. Electrons generated at the cathode are sampled from a semi-Maxwellian VDF with a mean energy of 4.5 eV and the flux distribution over the boundary is assumed uniform. The electrical connection between anode and cathode through an external circuit imposes continuity of discharge current, I_d, which is satisfied at any instant of the simulation. SEE model considers a linear SEE yield law,

$$\delta_s(\mathcal{E}_{e\mathrm{W}t}) = \mathcal{E}_{e\mathrm{W}t}/\mathcal{E}_c, \tag{3}$$

with $\mathcal{E}_{e\mathrm{W}t}$ the impacting electron energy and $\mathcal{E}_c = 50$ eV the material cross-over energy. Secondary electrons are sampled from a semi-Maxwellian VDF with an average energy of 0.4 eV.

Neutrals, n, are described as a background fluid with a given axial fluid velocity $u_{zn} = 300$ m/s and axially dependent density $n_n(z)$. In order to avoid simulating long time-scales, associated to the slow neutral dynamics, the simple neutral depletion law presented in Ref. 6 was used within the thruster channel

$$n_n(z) = \frac{\dot{m} - \dot{m}_{zi}}{u_{zn} A m_i}, \tag{4}$$

Copyright 2024 by the Electric Rocket Propulsion Society. All rights reserved.

where m_i is the ion mass, A is the channel cross section area, $\dot{m}_{zi}$ is the axial ion mass flow and $\dot{m} = 17.59$ mg/s is the injected neutral mass flow at the back wall. Note that Eq. (4) conserves the total mass flow and accounts for both, volumetric ionization and wall recombination. In the near plume, n_n is assumed constant.

Collisions include include elastic, excitation and ionization $e - n$ events. Excluding ionization, ions are considered collisionless. The collisional cross-sections were retrieved from the Biagi database[20] available in LXCat. Ideally, all excitation collisions should be implemented in the simulation code. However, in order to make simulations computationally lighter, it is convenient to define an effective excitation collision which groups the effect of all these processes, with an average energy loss $\Delta\mathcal{E}_{exc} = -10$ eV. Due to the axial-radial nature of the simulation, azimuthal instabilities inducing cross-field electron transport cannot be resolved. Alternatively, an empirical model is used, and their effect is included as an isotropic anomalous collisionality

$$\nu_{ano} = \alpha_{ano}(z, r)\, \omega_{ce}. \tag{5}$$

Such anomalous transport law has been extensively used in previous literature[2,21,22] with a step-out function for the anomalous coefficient $\alpha_{ano}(z, r)$

$$\alpha_{ano} = \alpha_{ano1} + \frac{\alpha_{ano2} - \alpha_{ano1}}{2}\left[1 + \tanh\left(\frac{\lambda - \lambda_t}{l_t}\right)\right]. \tag{6}$$

Equation 6 is expressed in terms of the magnetic stream function $\lambda(z, r)$. Parameters $\alpha_{ano1} = 0.012$ and $\alpha_{ano2} = 0.048$ are the inner and outer anomalous transport coefficients. The transition is defined at the magnetic field line with $\lambda_t = \lambda(1.49L, r_{\rm M})$ and the thickness is given by $l_t = 1/30$ Gm^2. The anomalous collisionality map is displayed in Fig. 2(d). All collisions are implemented using Monte Carlo Collision (MCC) algorithms.

Regarding numerical parameters, a square mesh with cell size $\Delta z = \Delta r = 200$ μm has been employed. The simulation time-step is $\Delta t = 15$ ps and the total simulated time is 60 μs. The simulations shown here were run using 20 cores on a workstation with 2 sockets, each one with 20 cores Intel(R) Xeon(R) Gold 6230 CPU @ 2.10 GHz. The simulation time is approximately one week.

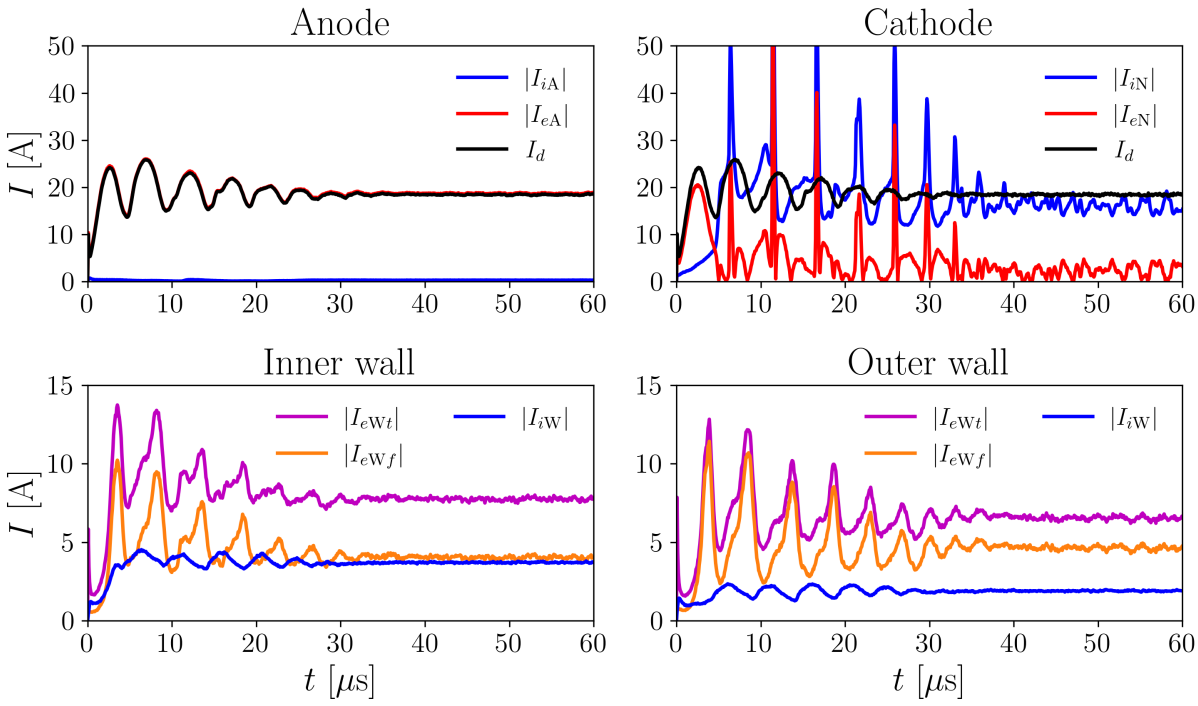

Figure 3. Time evolution of electron and ion currents to important boundary surfaces: (a) anode, (b) virtual cathode, (c) inner dielectric wall, and (d) outer dielectric wall of the simulated thruster.

Copyright 2024 by the Electric Rocket Propulsion Society. All rights reserved.

III. The reference simulation

The simulation starts with a filled domain and Maxwellian VDFs for electrons and ions. Initially, identical particle densities and temperatures for electrons and ions are considered, with $n_{e0} = n_{i0} = 4 \cdot 10^{17}$ m^{-3} and $T_{e0} = T_{i0} = 1$ eV. The time evolution of electron and ion currents to different boundary surfaces are plotted in Fig. 3. In Fig. 3(a) the electric current to the anode is dominated by electrons, with a marginal contribution of ions, as it is the desirable situation in a HET. Yet some ions must reach the anode surface to ensure good plasma attachment to the anode. Anode and cathode satisfy continuity of the discharge current, I_d. The ion and electron currents to the cathode are displayed in Fig. 3(b). The electron current is the resultant of injected electrons through the cathode and those reaching the boundary. Currents to the inner and outer dielectric walls are displayed in Figs. 3(c) and (d) respectively. Here, the current of bulk plasma electrons reaching the walls, $I_{e\mathrm{W}t}$, and the current of secondary electrons emitted from the material surface, $I_{e\mathrm{W}f}$ have been plotted separately. At steady-state, the dielectric condition imposes that the net electric current reaching the walls is zero. It can be observed that currents to the inner and outer walls are rather different. This asymmetry is induced by cylindrical effects on the discharge and the asymmetric and curved magnetic field topology. All the magnitudes in Fig. 3 exhibit some current oscillations with a period of some μs, which corresponds with time-scales of the ion dynamics. Such oscillations are stronger initially but are damped over time. After approximately 40 μs, steady-state is reached. Hereon, only the stationary plasma response will be discussed. In order to mitigate the PIC related noise, stationary results are time-averaged

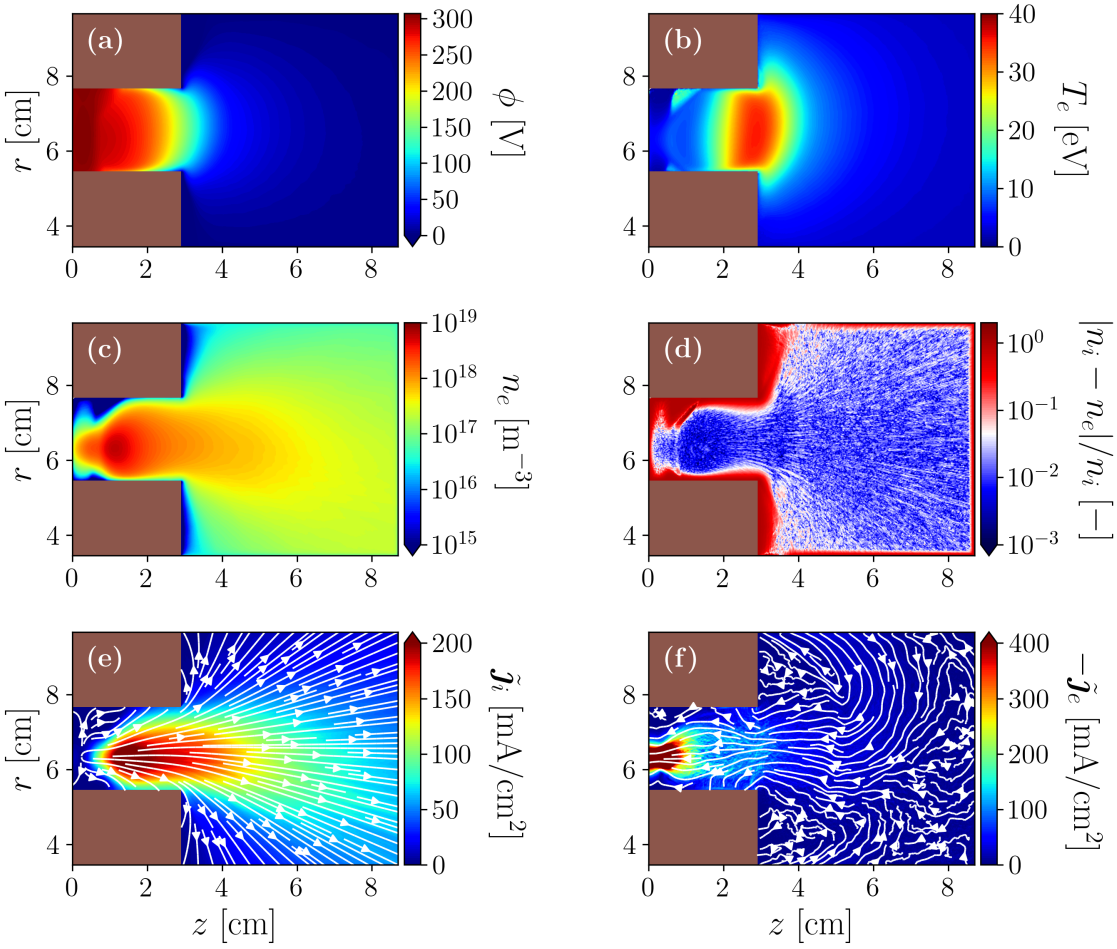

Figure 4. Maps of the main macroscopic variables characterizing the reference case simulation at steady-state: (a) electric potential, (b) electron temperature, (c) electron density, (d) neutrality ratio, (e) and (f) longitudinal ion and electron current densities respectively.

Copyright 2024 by the Electric Rocket Propulsion Society. All rights reserved.

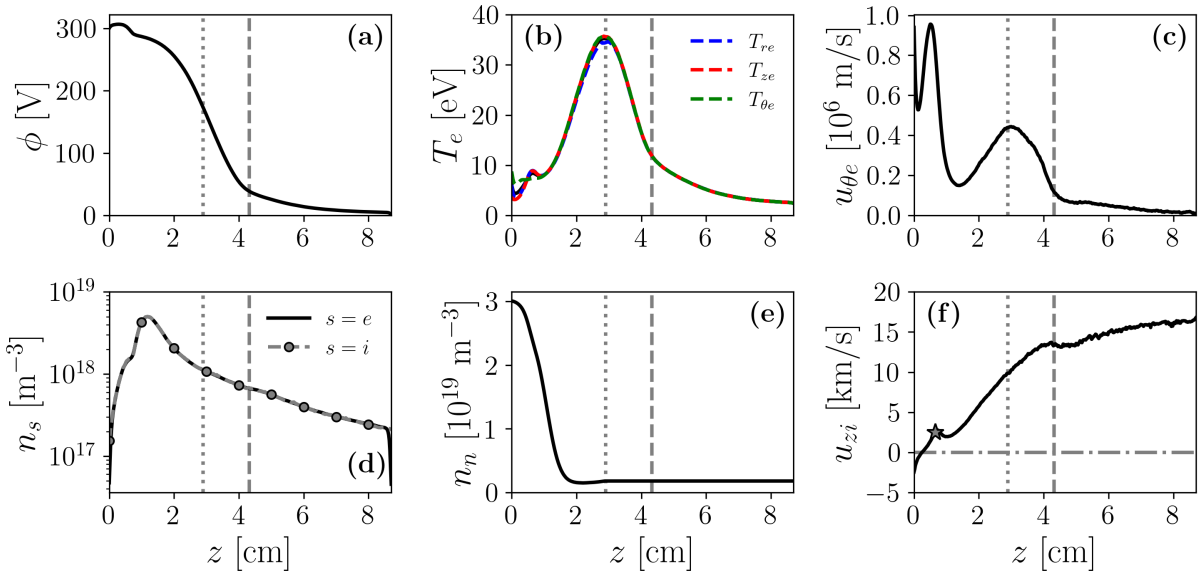

Figure 5. Axial profiles of steady-state macroscopic variables for the reference case simulation at the mean radius, r_M: (a) electric potential, (b) scalar electron temperature and directional temperatures, (c) azimuthal fluid electron velocity, (d) ion and electron density, (e) neutral density, and (f) axial fluid ion velocity. The star marker in plot (f) shows the location of the axial ion sonic point, with $c_s = \sqrt{T_e/m_i}$ the local sonic speed. The dotted vertical line marks the location of the thruster exit and the dashed vertical line denotes the anomalous diffusion transition.

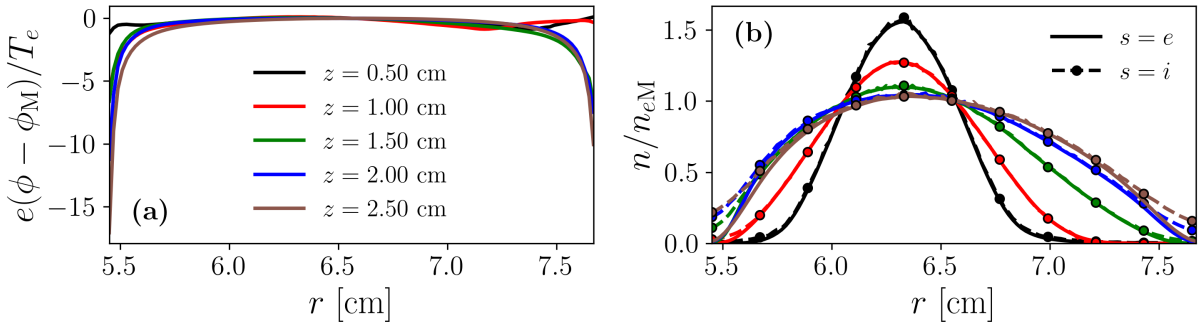

Figure 6. Radial profiles of steady-state macroscopic variables for the reference case simulation at different axial locations: (a) non-dimenional electric potential, and (b) non-dimensional ion and electron densities.

over the last 7.5 μs of the simulation. At steady-state, the number of simulated particles per species is over one million.

Figure 4 plots 2D maps of relevant macroscopic magnitudes at steady-state conditions and Fig. 5 shows axial profiles along r_M. In agreement with Refs. 13, 14, the electron temperature is rather isotropic in most of the domain. In the near exit region, where the magnetic field is almost radial, the plasma response follows the expected trends well known from 1Dz fluid models.[23,24] However, close to the anode the plasma response has important 2D features. Figure 4(c) shows a a sharp change in n_e at the location of the magnetic field line that joins the dielectric walls with the anode surface (see Fig. 2(c)). According to Fig. 4(d), this region is non-neutral and Fig. 4(c) shows an increase in T_e. However, the low number of particles (associated to the very low density there) and the augmentation factor f_D make difficult to draw strong conclusions. As a consequence, further research is needed to fully understand the local plasma behavior there. The electron current density near the anode is concentrated around the center of the channel and streamlines also follows

Copyright 2024 by the Electric Rocket Propulsion Society. All rights reserved.

the shape of the magnetic field. In the region of curved magnetic field, ion streamlines show that few particles are capable of reaching the walls. In turn, this is mainly driven by the electric potential shape, in Fig. 5 (a).

Radial profiles of electric potential and plasma density at five different axial locations are plotted in Fig. 6. For a better comparison, such profiles are presented in non-dimensional form, $n_e/n_{e\mathrm{M}}$ and $e(\phi-\phi_{\mathrm{M}})/T_e$. Both magnitudes exhibit radial asymmetries that can be mainly related to asymmetries in $\boldsymbol{B}$ and become more evident in regions with a significantly oblique magnetic field. Radial profiles at $z = 1.5, 2.0, 2.5$ cm have a common behavior and resemble those obtained with a 1Dr PIC model of the discharge assuming a purely radial magnetic field.[19,25] However, for $z = 0.5, 1.0$ cm, the potential profile is almost flat and the plasma density is concentrated in the channel center, away from the thruster walls. In these regions the magnetic field has a larger axial component, which prevents the plasma from reaching the walls. These results follow the same qualitative trends as in Ref. 13 for magnetic lenses with high curvature, featuring strong density gradients in the quasineutral plasma. A novelty of the results shown here is that the simulation suggests that that Debye sheaths may collapse for a grazing magnetic incidence. A more detailed investigation is required to get a better understanding of this interesting phenomenon.

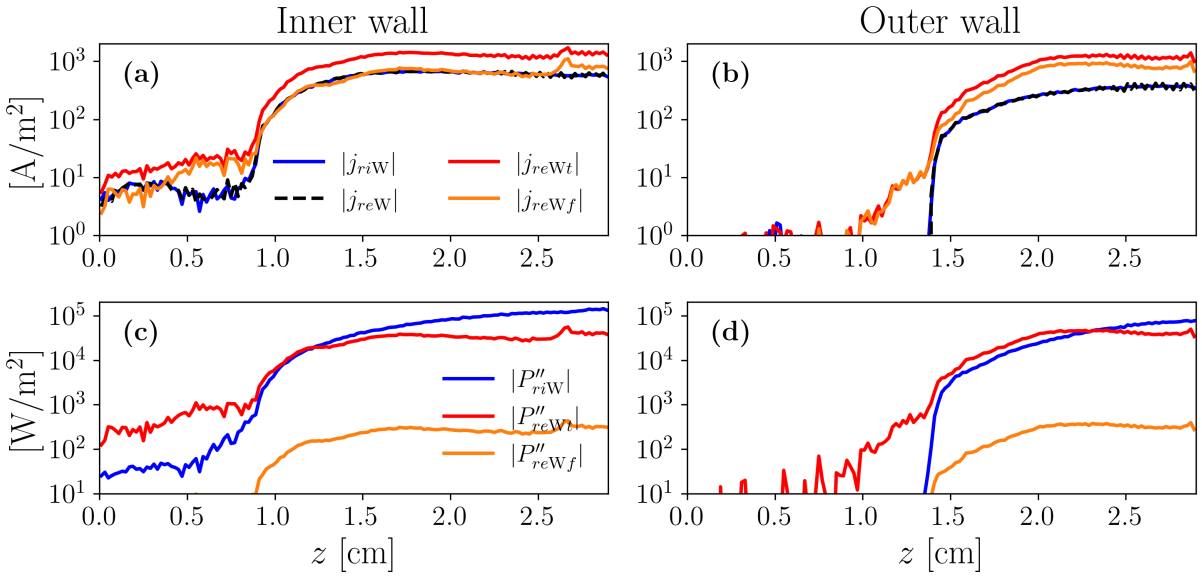

Figure 7. Wall interaction magnitudes at the inner wall, left column plots, and outer wall, right column plots: (a), (b) ion current density to the wall $j_{ri\mathrm{W}}$, electron current density to the wall $j_{re\mathrm{W}t}$, and electron current density from the wall (SEE) $j_{re\mathrm{W}f}$; and (c), (d) ion energy flux to the wall $P''_{ri\mathrm{W}}$, electron energy flux to the wall $P''_{re\mathrm{W}t}$, and electron (SEE) energy flux from the wall $P''_{re\mathrm{W}f}$.

Wall interaction magnitudes are summarized in Fig. 7. As expected, at steady state, the dielectric walls are locally current free. Therefore, the net axial electric current must be conserved at every axial section of the thruster channel

$$I_d = I_{zi} + I_{ze} = \text{constant}. \tag{7}$$

It has been checked that Eq. (7) is well satisfied by the kinetic solution. SEE can be significant and promotes electron energy losses to the walls, since secondary electrons are much colder than electrons reaching the thruster walls. The effect of the magnetic field is clearly visible in all magnitudes and two different behaviors can be identified. Near the thruster exit, the magnetic field is approximately radial and the plasma fluxes to the walls are high. On the contrary, the curved magnetic field near the anode leads to much smaller particle and energy fluxes to the lateral walls. The approximate location where this transition occurs is where magnetic field lines no longer connect inner and outer walls but one of the walls with the anode (see Fig. 2(c)). Additionally, the stronger the magnetic field, the more the electron motion is inhibited.

Classical HETs implement a magnetic lens topology to reduce plasma fluxes to the walls. The rationale for this magnetic configuration is that, for cold electrons, isopotential lines should be coincident with magnetic field lines; thus, directing ions toward the channel center and away from the walls. However, in real thrusters

Copyright 2024 by the Electric Rocket Propulsion Society. All rights reserved.

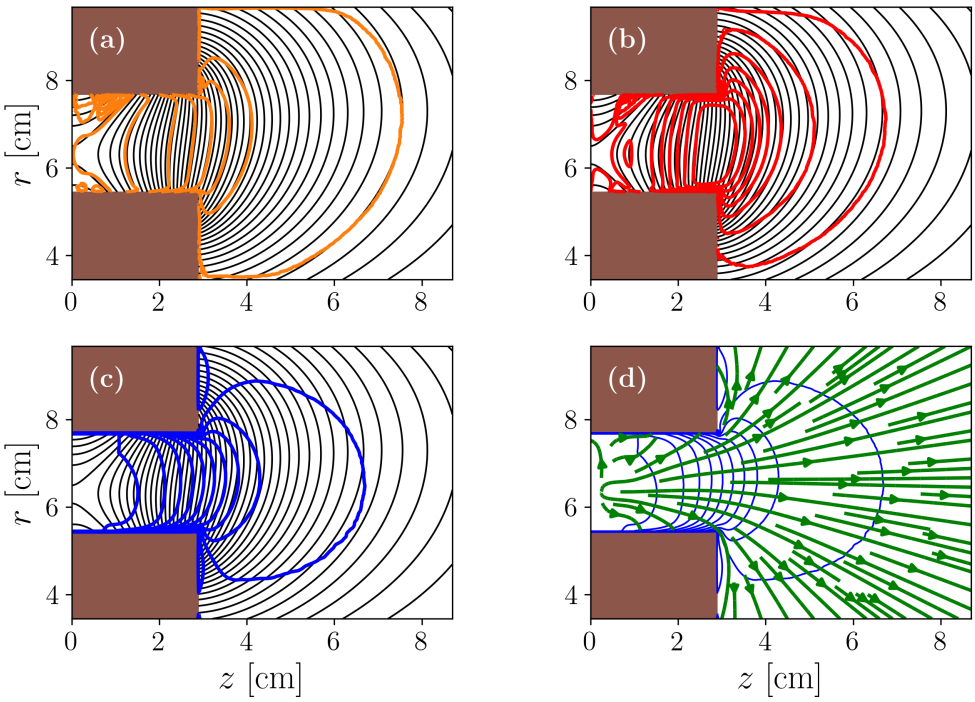

Figure 8. Comparison between kinetic results and theory: (a) magnetic field lines (λ =constant, black contour lines) and isolines of the thermalized potential (Φ =constant, orange contour lines); (b) magnetic field lines (black contour lines) and electron temperature (ϕ =constant, red contour lines); (c) magnetic field lines (black contour lines) and electric potential (blue contour lines); and (d) electric potential (blue contour lines) and ion streamlines (green streamlines).

the electron temperature is finite and this relation is not fulfilled. Alternatively, Morozov and Savelyev[26] proposed that the magnitude that is conserved along the magnetic field lines is the so called thermalized potential and not the electric potential itself. Based on the on the assumption of isothermal magnetic field lines, the thermalized potential is defined as

$$\Phi = \phi - \frac{T_e}{e} \ln(n_e/n_{ref}). \tag{8}$$

The assumption T_e =constant along a magnetic line relies on the large thermal conductivity parallel to the magnetic field predicted by fluid theory. A more rigorous derivation for the thermalized potential, including an expression for non-isothermal magnetic lines, can be found in Ref. 4.

Figure 8 compares the aforementioned theory, based on a fluid formulation, with the kinetic plasma response. Isolines for the magnetic field stream function (λ =constant) and thermalized potential are plotted in Fig. 8(a), showing a good correlation between them. Deviations from the theoretical result are due to cylindrical effects, electron inertia and temperature variations along magnetic field lines. Figure 8(b) depicts electron temperature and magnetic field lines. Although T_e approximately follows the magnetic topology, magnetic field lines exhibit some temperature variations. Electric potential isolines and the magnetic topology are displayed in Fig. 8(c), showing a large disagreement. Figure 8(d) shows ion streamlines and the electric potential map. Ion streamlines are approximately perpendicular to the electric potential isosurfaces in the thruster channel, which indicates that particle trajectories follow the direction of the electric field. Out of the thruster channel this is not fulfilled due to the large ion inertia and weaker variations in the potential. Furthermore, it can be observed that no ion focusing occurs and ions are always accelerated towards the walls. However, the magnetic field curvature can affect the degree of ion radial defocusing.

Copyright 2024 by the Electric Rocket Propulsion Society. All rights reserved.

IV. Radial magnetic field

When analyzing the reference simulation we have discussed on the central role of the magnetic field topology shaping the distribution of plasma magnitudes and reducing particle and energy fluxes to the walls. In order to further analyze the effect of the magnetic field shape, a scenario with a purely radial magnetic field is considered next. Although it is not physically accurate, this approximation has been applied in previous kinetic studies.[6–8] The divergence-free magnetic field for this simulation is

$$\boldsymbol{B}(z,r) = B_{\mathrm{M}}(z)\frac{r_{\mathrm{M}}}{r}\mathbf{1}_r, \tag{9}$$

where B_{M} is the value of B at r_{M} for the reference case, Fig. 2(b).

Figure 9 show 2D maps of the main macroscopic plasma magnitudes for the simulation with a purely radial magnetic field. The plasma response features similar trends to those reported in Ref. 6 and shows large differences with respect to Fig. 4. Figure 10 depicts the radial distribution of n_e and ϕ in non-dimensional form at different axial sections for the radial magnetic field case. Here, the sheath collapse present in Fig. 6 does not appear. Radial asymmetries in the discharge are no longer determined by asymmetries in the magnetic field topology. Alternatively, they are driven by cylindrical expansion terms. Domínguez-Vázquez et al.[19] already reported that azimuthal electron inertia and anisotropy in the electron temperature induce deviations in the electron response from a standard Boltzmann relation. Such terms, proportional to $1/r$, generate a radially outwards macroscopic force pushing the maximum plasma density closer to the upper wall.

Figure 11 compare the ion current to the walls in reference case and the simulation with a radial magnetic field. Values in the near exit region remain similar, but large discrepancies are found close to the anode. These are motivated by the drastic change in magnetic field curvature between the two cases. Near the anode, the plasma fluxes to the lateral walls are much larger in the scenario with a radial magnetic field

Description and symbol	**Reference case**	**Radial magnetic field**
Discharge current, I_d	18.42 A	18.55 A
Ion current to the anode, $\lvert I_{i\mathrm{A}}\rvert$	0.29 A	0.12 A
Electron current to the anode, $\lvert I_{e\mathrm{A}}\rvert$	18.71 A	18.67 A
Ion current to the inner wall, $\lvert I_{i\mathrm{W}_1}\rvert$	3.71 A	3.02 A
Electron current to the inner wall, $\lvert I_{e\mathrm{W}_1 t}\rvert$	7.75 A	5.66 A
SEE current from the inner wall, $\lvert I_{e\mathrm{W}_1 f}\rvert$	4.04 A	2.65 A
Ion current to the outer wall, $\lvert I_{i\mathrm{W}_2}\rvert$	1.90 A	4.34 A
Electron current to the outer wall, $\lvert I_{e\mathrm{W}_2 t}\rvert$	6.52 A	10.53 A
SEE current from the outer wall, $\lvert I_{e\mathrm{W}_2 f}\rvert$	4.62 A	6.20 A
Discharge power, $I_d V_d$	5525 W	5565 W
Ion power to the anode, $P_{i\mathrm{A}}$	2 W	< 1 W
Electron power to the anode, $P_{e\mathrm{A}}$	402 W	425 W
Ion power to the inner wall, $P_{i\mathrm{W}_1}$	491 W	372 W
Electron power to the inner wall, $P_{e\mathrm{W}_1 t}$	202 W	132 W
SEE power from the inner wall, $P_{e\mathrm{W}_1 f}$	2 W	1 W
Ion power to the outer wall, $P_{i\mathrm{W}_2}$	261 W	503 W
Electron power to the outer wall, $P_{e\mathrm{W}_2 t}$	231 W	310 W
SEE power from the outer wall, $P_{e\mathrm{W}_2 f}$	2 W	2 W

Table 2. Current and power deposited at different surfaces.

Copyright 2024 by the Electric Rocket Propulsion Society. All rights reserved.

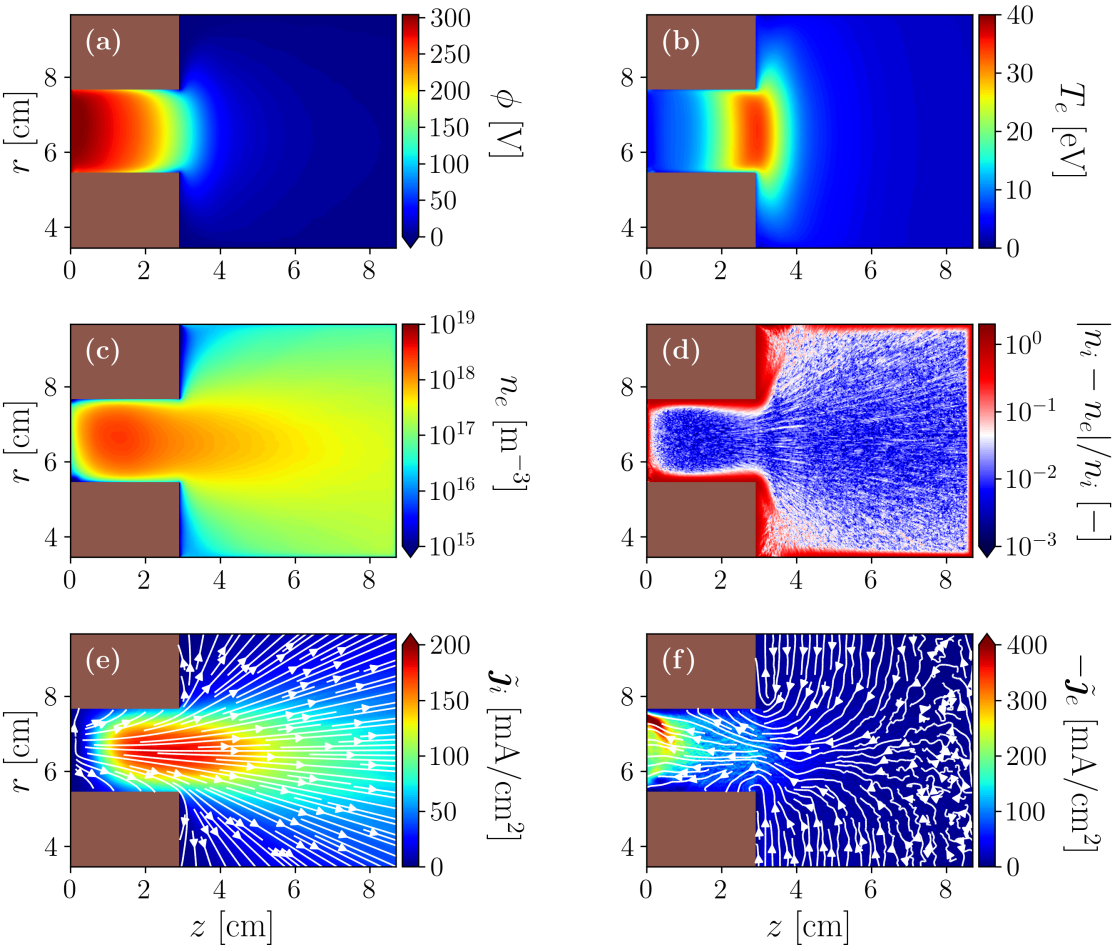

Figure 9. Maps of the main macroscopic variables for the simulation with a purely radial magnetic field at steady-state: (a) electric potential, (b) electron temperature, (c) electron density, (d) neutrality ratio, (e) and (f) longitudinal ion and electron current densities respectively.

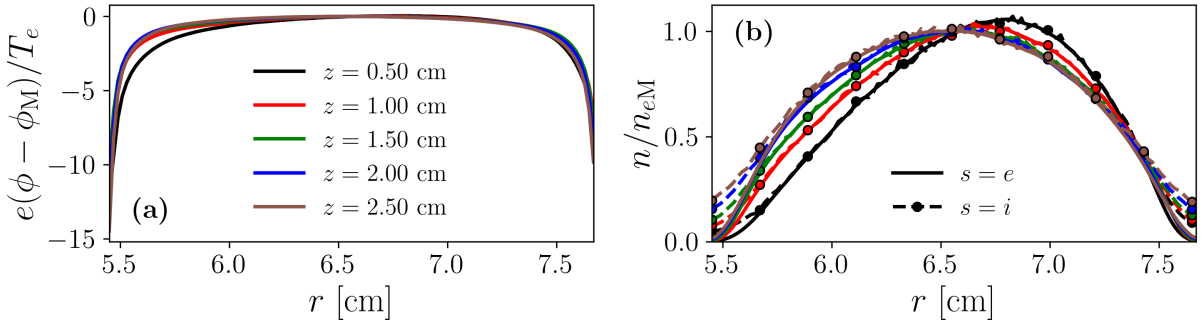

Figure 10. Radial profiles of steady-state macroscopic variables for the simulation with a purely radial magnetic field: (a) non-dimenional electric potential, and (b) non-dimensional ion and electron densities.

than in the reference case. Table 2 gathers the integrated currents and power deposited at different surfaces. In both cases the discharge current remains similar, but with a lower amount of ions reaching the anode for the case with a radial magnetic field. The stronger the radial magnetic field, the lower ion current to the

Copyright 2024 by the Electric Rocket Propulsion Society. All rights reserved.

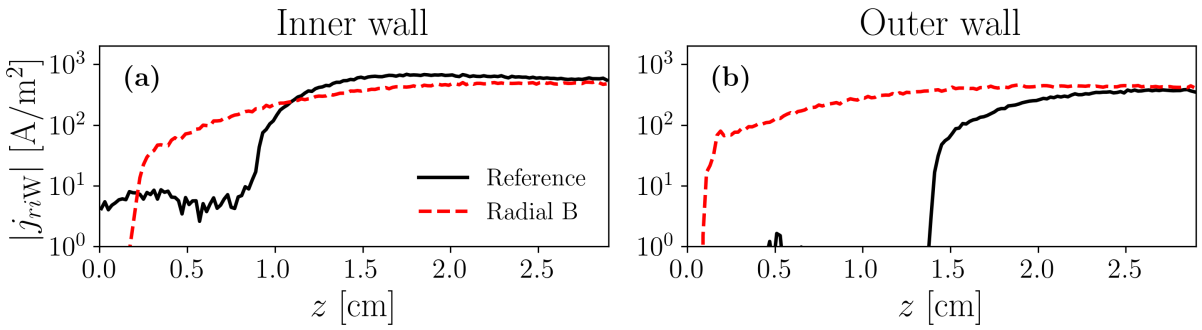

Figure 11. Wall interaction magnitudes for the reference case and the simulation with a purely radial magnetic field: (a) and (b) ion current densities to the wall for the inner and outer wall respectively.

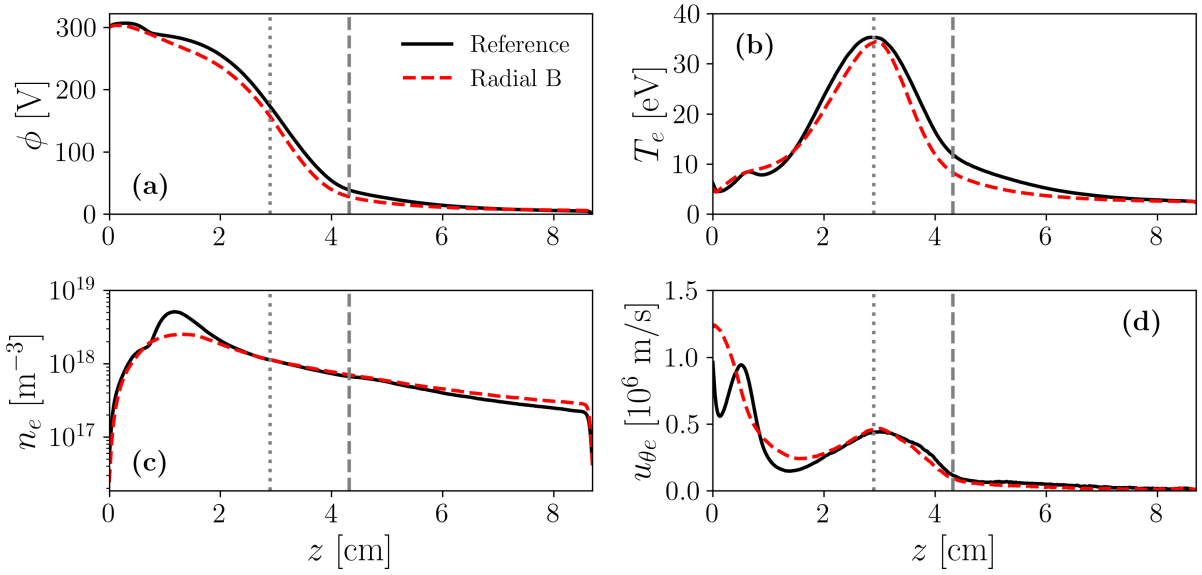

Figure 12. Comparison of axial profiles of steady-state macroscopic variables at r_M for the reference case and the simulation with a purely radial magnetic field: (a) electric potential, (b) electron temperature, (c) electron density, and (d) azimuthal electron fluid velocity. The dotted vertical line marks the location of the thruster exit and the dashed vertical line denotes the anomalous diffusion transition.

anode.[24] Asymmetries in current and power to the dielectric walls are opposite in both simulations. For the scenario with a radial magnetic field, asymmetries in the discharge follow similar trends to those reported in Ref. 25, with larger plasma currents to the outer wall. The total ion current and total power to both walls is lower in the reference case. Nonetheless, the difference in power deposited at both walls between the simulations is small. This is because the oblique magnetic field in the reference case is protecting the lateral walls close to the anode, where electrons are colder and ions have not accelerated. Thus, the magnetic field is protecting the walls from low energy particles. Particles impinging the walls close to the exit are contributing more to the power deposition because they are more energetic, and at that region the magnetic field is almost radial for both cases.

Figure 12 compares the results of both simulations in terms of axial profiles of macroscopic plasma variables along r_M. Although it is clear that the change in magnetic topology has affected the discharge, results along the channel mid radius are similar. This is reasonable because $\boldsymbol{B}$ is not too far from radial at r_M.

Copyright 2024 by the Electric Rocket Propulsion Society. All rights reserved.

V. Conclusions

The 2D axial-radial PIC model of Ref. 6 (PICASO) has been improved to analyze more realistic HET discharges, considering cylindrical effects and a curved magnetic field topology. Electrons and singly charged ions are treated as two populations of macroparticles. Alternatively, neutrals are modeled as a background fluid. Ionization, excitation and elastic electron-neutral collisions are simulated with MCC algorithms. An empirical model for anomalous diffusion is included to account for electron transport induced by azimuthal instabilities. Acceleration techniques, such as a steady-state law for neutrals and an augmented vacuum permittivity, have been used to reduce the required computational cost.

The reference case simulates a virtual 5 kW class HET. The magnetic topology features a large curvature near the anode and is almost radial near the exit. The time-evolution of currents to different domain boundaries shows convergence converge and steady-state solution is analyzed. Near the thruster exit, the plasma follow the expected trends in a HET discharge. Magnetic field lines approximately coincide with isolines of the thermalized potential and show mild temperature variations. On the other hand, isopotential lines of ϕ do not match with the magnetic field topology and we do not observe ion focusing. Simulation results indicate that that the curved magnetic field topology near the anode effectively reduces particle and energy fluxes to the lateral dielectric walls. Radial profiles of the electric potential and plasma density suggest that the Debye sheath may vanish for grazing magnetic incidence. However, further research is required to draw conclusions on this phenomenon.

A scenario with a purely radial magnetic field is analyzed as well. In this case asymmetries in the discharge arise due to cylindrical expansion terms in the radial momentum equation,[19] which push the peak plasma density towards the outer wall. As a consequence, particle fluxes to the outer wall are larger than to the inner wall, in agreement with Ref. 25. The lack of magnetic field curvature near the anode leads to significantly higher fluxes to the dielectric walls in this scenario compared to the reference case. Nonetheless, macroscopic magnitudes along the mean channel radius are similar in both simulations.

The results obtained in this work have proven the capabilities the 2Dzr PIC code to study realistic HET discharges. We expect to extend this work with the analysis of magnetic-shielded topologies. Furthermore, the comparison with the hybrid model HYPHEN is also planned.

Appendix

In order to check the robustness of the results commented in previous Sections, additional simulations have been performed. The effect of different domain sizes and anomalous transport models are addressed in this appendix. For the sake of comparison, the reference simulation is named Case 1 here.

A. Domain size effect (Cases 2 and 3)

The plume expansion into vacuum is truncated at the downstream boundary of the simulation domain. In order to evaluate the domain size effect, two additional simulations have been performed: one with a smaller domain size (Case 2) and another with a radially extended plume region (Case 3). Figure 13 plots the different domain sizes for Cases 1, 2 and 3. Furthermore, the time-step for Case 2 was reduced by a factor two to evaluate the effect of Δt in the results.

Figure 14 provides a quantitative comparison of axial profiles of relevant macroscopic variables along r_{M}, showing good agreement. The three cases yield almost identical results inside the HET channel. Only mild differences are observed in the plume region and peak value of the electron temperature. Macroscopic magnitudes in the thruster channel and wall interaction parameters are weakly affected by the size of the near plume in the simulation model as long as the downstream boundary is not too close to the channel exit. Moreover, Case 2, featuring a smaller time-step, does not show changes in the the numerical results. Thus, reducing Δt does not modify the solution.

B. Constant anomalous transport coefficient (Case 4)

In this Section we evaluate how the different anomalous transport models affect the plasma response. For this purpose we compare the results of the reference simulation (Case 1) and a simulation that assumes a constant anomalous transport coefficient $\alpha_{ano} = \alpha_{ano1} = 0.012$ (Case 4).

Copyright 2024 by the Electric Rocket Propulsion Society. All rights reserved.

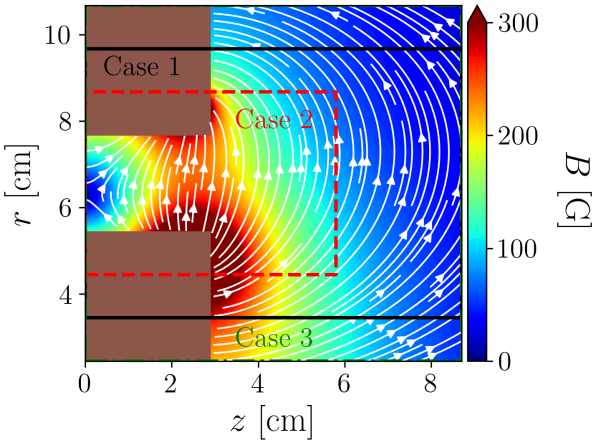

Figure 13. Magnetic field topology and domain sizes for different simulations: reference simulation (Case 1, solid black line), small simulation domain (Case 2, dashed red line) and radially extended plume region (Case 3, dash-dotted green line, corresponding with figure limits).

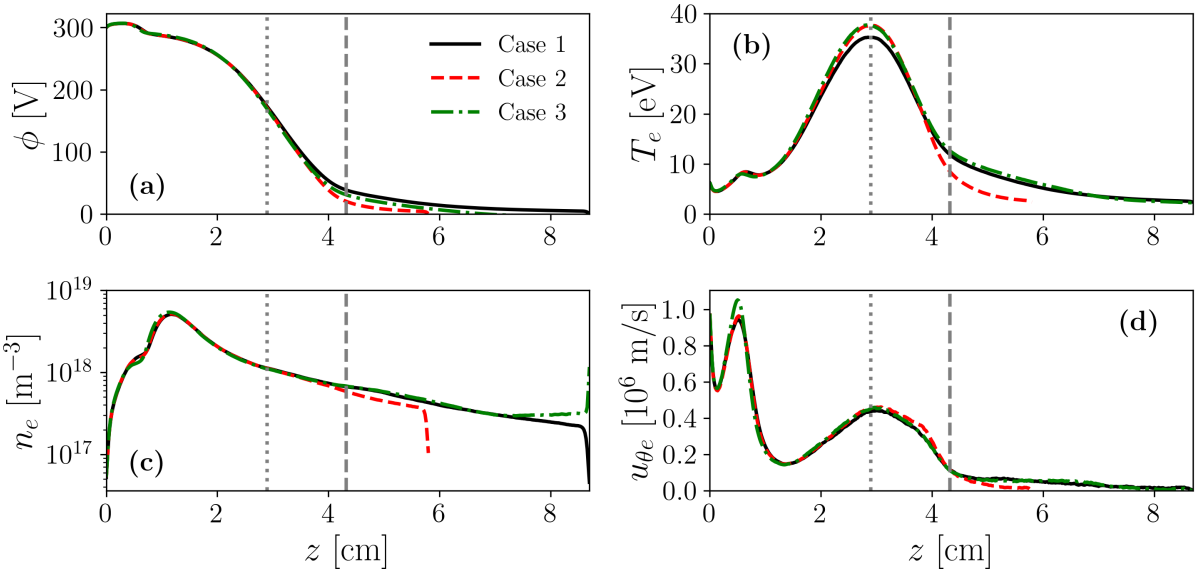

Figure 14. Comparison of axial profiles of steady-state macroscopic variables at the mean radius for Cases 1, 2 and 3: (a) electric potential, (b) electron temperature, (c) electron density, and (d) azimuthal electron fluid velocity. The dotted vertical line marks the location of the thruster exit and the dashed vertical line denotes the anomalous diffusion transition.

The simulation results suggest that there are not major changes in the plasma response and wall interaction magnitudes inside the thruster channel, although there are some quantitative changes in the near plume region. Figure 15 compares axial profiles of macroscopic magnitudes along r_{M} for Cases 1 and 4. Indeed, the changes follow the expected trend, with larger gradients in macroscopic plasma magnitudes in the near plume for Case 4, with a lower collisionality there.

Copyright 2024 by the Electric Rocket Propulsion Society. All rights reserved.

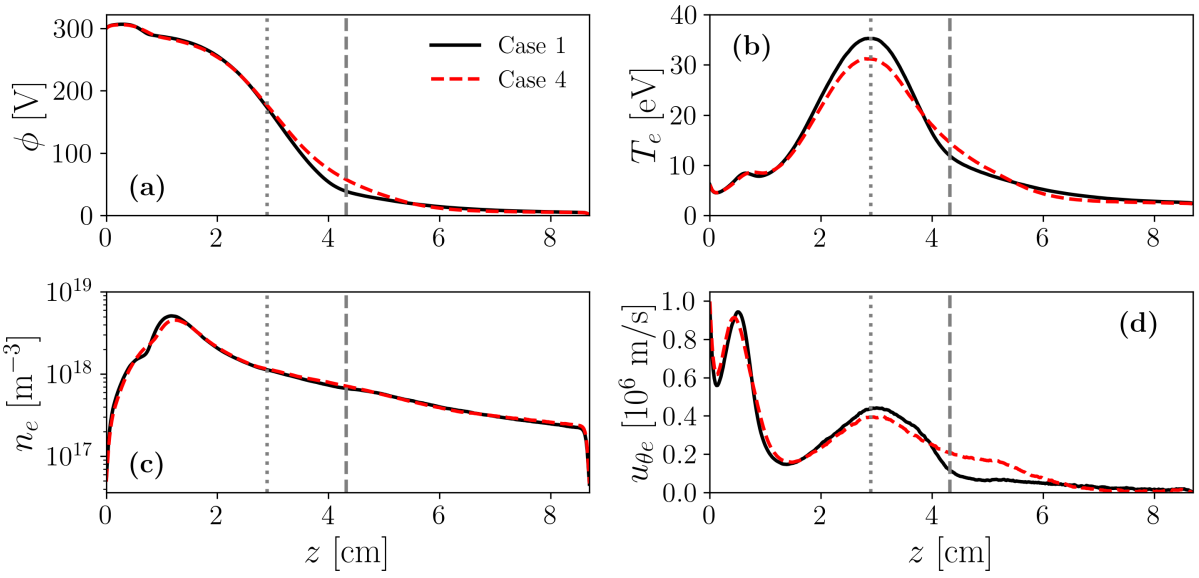

Figure 15. Comparison of axial profiles of steady-state macroscopic variables at the mean radius for Cases 1 and 4: (a) electric potential, (b) electron temperature, (c) electron density, and (d) azimuthal electron fluid velocity. The dotted vertical line marks the location of the thruster exit and the dashed vertical line denotes the anomalous diffusion transition for Case 1.

Acknowledgments

This work has been supported by the R&D project HEEP (PID2022-140035OB-I00) funded by MCIN/AEI/10.13039/501100011033 and by "ERDF A way of making Europe". A. Marín-Cebrián thanks the financial support by MCIN/AEI/10.13039/501100011033 under grant FPU20/02901. The contribution of E. Bello-Benítez was supported by the European Research Council under the European Union's Horizon 2020 research and innovation programme (project ZARATHUSTRA, grant agreement No 950466).

References

[1]Ortega, A., Mikellides, I., Sekerak, M., and Jorns, B., "Plasma simulations in 2-D (r-z) geometry for the assessment of pole erosion in a magnetically shielded Hall thruster," *Journal of Applied Physics*, Vol. 125, No. 3, 2019.

[2]Perales-Díaz, J., Domínguez-Vázquez, A., Fajardo, P., Ahedo, E., Faraji, F., Reza, M., and Andreussi, T., "Hybrid plasma simulations of a magnetically shielded Hall thruster," *Journal of Applied Physics*, Vol. 131, No. 10, 2022, pp. 103302.

[3]Bittencourt, J., *Fundamentals of plasma physics*, Springer, Berlin, Germany, 2004.

[4]Ahedo, E., "Using electron fluid models to analyze plasma thruster discharges," *Journal of Electric Propulsion*, Vol. 2, No. 1, 2023, pp. 2.

[5]Taccogna, F. and Garrigues, L., "Latest progress in Hall thrusters plasma modelling," *Reviews of Modern Plasma Physics*, Vol. 3, No. 1, 2019, pp. 12.

[6]Marín-Cebrián, A., Bello-Benítez, E., Domínguez-Vázquez, A., and Ahedo, E., "Non-Maxwellian electron effects on the macroscopic response of a Hall thruster discharge from an axial–radial kinetic model," *Plasma Sources Science and Technology*, Vol. 33, No. 2, feb 2024, pp. 025008.

[7]Taccogna, F., Schneider, R., Longo, S., and Capitelli, M., "Kinetic simulations of a plasma thruster," *Plasma Sources Science and Technology*, Vol. 17, No. 2, 2008, pp. 024003.

[8]Liu, H., Wu, B., Yu, D., Cao, Y., and Duan, P., "Particle-in-cell simulation of a Hall thruster," *Journal of Physics D: Applied Physics*, Vol. 43, No. 16, 2010, pp. 165202.

[9]Kim, V., "Main physical features and processes determining the performance of stationary plasma thrusters," *J. Propulsion Power*, Vol. 14, No. 5, 1998, pp. 736–743.

[10]Hofer, R. and Gallimore, A., "The role of magnetic field topography in improving the performance of high-voltage Hall thrusters," *38th Joint Propulsion Conference*, AIAA 2002-4111, Indianapolis, IN, 2002.

[11]Liu, J., Li, H., Hu, Y., Liu, X., Ding, Y., Wei, L., Yu, D., and Wang, X., "Particle-in-cell simulation of the effect of curved magnetic field on wall bombardment and erosion in a Hall thruster," *Contributions to Plasma Physics*, Vol. 59, No. 8, 2019, pp. e201800001.

[12]Ma, D., Zeng, D., Wang, L., Ding, Y., Wei, L., Li, H., and Yu, D., "Numerical simulation study on the influence of

Copyright 2024 by the Electric Rocket Propulsion Society. All rights reserved.

channel geometry on discharge characteristics of low-power magnetically shielded Hall thrusters," *Vacuum*, Vol. 180, 2020, pp. 109547.

[13]Marín-Cebrián, A., Domínguez-Vázquez, A., Fajardo, P., and Ahedo, E., "Kinetic plasma dynamics in a radial model of a Hall thruster with a curved magnetic field," *Plasma Sources Science and Technology*, Vol. 31, No. 11, nov 2022, pp. 115003.

[14]Miedzik, J., Barral, S., and Daniłko, D., "Influence of oblique magnetic field on electron cross-field transport in a Hall effect thruster," *Physics of Plasmas*, Vol. 22, No. 4, 2015, pp. 043511.

[15]Reza, M., Faraji, F., and Knoll, A., "Influence of the magnetic field's curvature on the radial-azimuthal dynamics of a Hall thruster plasma discharge with different propellants," *arXiv preprint arXiv:2309.00565*, 2023.

[16]Domínguez-Vázquez, A., Zhou, J., Sevillano-González, A., Fajardo, P., and Ahedo, E., "Analysis of the electron downstream boundary conditions in a 2D hybrid code for Hall thrusters," 37^{th} *International Electric Propulsion Conference*, No. IEPC-2022-338, Electric Rocket Propulsion Society, Boston, MA, June 19-23, 2022.

[17]Birdsall, C. and Langdon, A., *Plasma Physics via Computer Simulation*, Institute of Physics Publishing, Bristol, 1991.

[18]Szabo, J., Warner, N., Martinez-Sanchez, M., and Batishchev, O., "Full particle-in-cell simulation methodology for axisymmetric Hall effect thrusters," *Journal of Propulsion and Power*, Vol. 30, No. 1, 2014, pp. 197–208.

[19]Domínguez-Vázquez, A., Taccogna, F., and Ahedo, E., "Particle modeling of radial electron dynamics in a controlled discharge of a Hall thruster," *Plasma Sources Science and Technology*, Vol. 27, No. 6, 2018, pp. 064006.

[20]Stephen Francis Biagi, "Cross sections extracted from PROGRAM MAGBOLTZ, VERSION 7.1 JUNE 2004," June 2004, [Online; accessed 5-July-2021].

[21]Hagelaar, G., Bareilles, J., Garrigues, L., and Boeuf, J., "Role of anomalous electron transport in a stationary plasma thruster simulation," *Journal of Applied Physics*, Vol. 93, No. 1, 2003, pp. 67–75.

[22]Koo, J. and Boyd, I., "Modeling of anomalous electron mobility in Hall thrusters," *Physics of Plasmas*, Vol. 13, 2006, pp. 033501.

[23]Ahedo, E., Gallardo, J., and Martínez-Sánchez, M., "Effects of the radial-plasma wall interaction on the axial Hall thruster discharge," *Physics of Plasmas*, Vol. 10, No. 8, 2003, pp. 3397–3409.

[24]Bello-Benítez, E. and Ahedo, E., "Stationary axial model of the Hall thruster plasma discharge: electron azimuthal inertia and far plume effects," *Plasma Sources Science and Technology*, Vol. 32, No. 11, 2023, pp. 115011.

[25]Marín-Cebrián, A., Domínguez-Vázquez, A., Fajardo, P., and Ahedo, E., "Macroscopic plasma analysis from 1D-radial kinetic results of a Hall thruster discharge," *Plasma Sources Science and Technology*, Vol. 30, No. 11, November 2021, pp. 115011.

[26]Morozov, A. and Savelyev, V., "Fundamentals of Stationary Plasma Thruster Theory," *Reviews of Plasma Physics, Vol. 21*, Kluwer Academic, New York, 2000.

Copyright 2024 by the Electric Rocket Propulsion Society. All rights reserved.